

The creation of a brain atlas for image guided neurosurgery using serial histological data

M. Mallar Chakravarty,^{a,*} Gilles Bertrand,^{a,b} Charles P. Hodge,¹
Abbas F. Sadikot,^{a,b} and D. Louis Collins^a

^aMcConnell Brain Imaging Centre, Montréal Neurological Institute, McGill University, 3801, University St., Montréal, Canada H3A 2B4

^bDivision of Neurosurgery, McGill University, Montreal, Canada

Received 14 April 2005; revised 21 July 2005; accepted 6 September 2005
Available online 9 January 2006

Digital and print brain atlases have been used with success to help in the planning of neurosurgical interventions. In this paper, a technique presented for the creation of a brain atlas of the basal ganglia and the thalamus derived from serial histological data. Photographs of coronal histological sections were digitized and anatomical structures were manually segmented. A slice-to-slice nonlinear registration technique was used to correct for spatial distortions introduced into the histological data set at the time of acquisition. Since the histological data were acquired without any anatomical reference (e.g., block-face imaging, post-mortem MRI), this registration technique was optimized to use an error metric which calculates a nonlinear transformation minimizing the mean distance between the segmented contours between adjacent pairs of slices in the data set. A voxel-by-voxel intensity correction field was also estimated for each slice to correct for lighting and staining inhomogeneity. The reconstructed three-dimensional (3D) histological volume can be viewed in transverse and sagittal directions in addition to the original coronal.

Nonlinear transformations used to correct for spatial distortions of the histological data were applied to the segmented structure contours. These contours were then tessellated to create three-dimensional geometric objects representing the different anatomic regions in register with the histological volumes. This yields two alternate representations (one histological and one geometric) of the atlas.

To register the atlas to a standard reference MR volume created from the average of 27 T1-weighted MR volumes, a pseudo-MRI was created by setting the intensity of each anatomical region defined in the geometric atlas to match the intensity of the corresponding region of the reference MR volume. This allowed the estimation of a 3D nonlinear transformation using a correlation based registration scheme to fit the atlas to the reference MRI.

The result of this procedure is a contiguous 3D histological volume, a set of 3D objects defining the basal ganglia and thalamus, both of which

are registered to a standard MRI data set, for use for neurosurgical planning.

© 2005 Elsevier Inc. All rights reserved.

Keywords: Brain atlas; Neurosurgery; MRI; Basal ganglia; Thalamus; Image guided neurosurgery; Functional neurosurgery; Segmentation; Registration

Introduction

Functional stereotactic neurosurgery is increasingly used for the treatment for movement disorders such as Parkinson's disease (Atkinson et al., 2002; Cohn et al., 1998; Cuny et al., 2002; Gross et al., 1999; Lenz et al., 1995; Lombardi et al., 2000; Samuel et al., 1998). While symptoms associated with Parkinson's disease (such as tremor, rigidity, bradykinesia, and impaired gait) can be treated pharmacologically, intractable cases require surgical intervention. For surgical candidates, this can include the introduction of recording or stimulating probes in deep cerebral structures and the creation of lesions in the thalamus (thalamotomy) (Atkinson et al., 2002; Gross et al., 1999; Lenz et al., 1995) or globus pallidus (pallidotomy) (Cohn et al., 1998; Lombardi et al., 2000; Samuel et al., 1998), or insertion of brain stimulation electrodes in the thalamus, globus pallidus, or subthalamic nucleus. Pre-surgical planning of these procedures requires a detailed analysis of the thalamus and the basal ganglia from pre-operative Computed Tomography (CT) and Magnetic Resonance Imaging (MR) volumes. However, cyto-architectonic boundaries between specific subcortical nuclei are often indistinguishable due to the limited contrast and resolution of these imaging modalities.

While new MR imaging and image processing techniques enable visualization of some nuclei (Deoni et al., 2005; Fujita et al., 2001; Starr et al., 1999), atlases are often used in conjunction with more standard imaging techniques to enhance the visualization of surgical targets for pre-operative planning and to accurately predict the optimal location of surgical targets in sub-cortical nuclei (Atkinson et al., 2002; Bertrand et al., 1973; Nowinski et al., 1997, 2000;

* Corresponding author. Fax: +1 514 398 2975.

E-mail address: mallar@bic.mni.mcgill.ca (M.M. Chakravarty).

¹ The late Charles Hodge was responsible for the photographic work shown in this manuscript, particularly with respect to the histological data acquisition. We are grateful for his contribution.

Available online on ScienceDirect (www.sciencedirect.com).

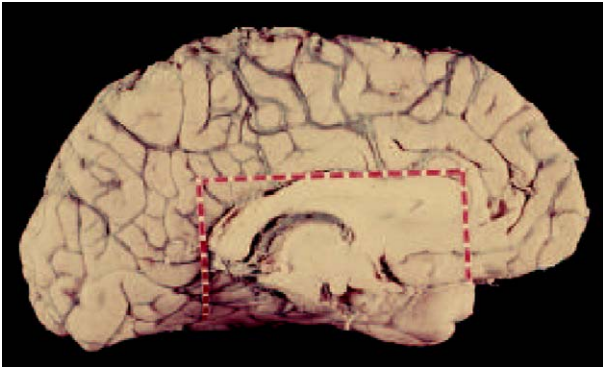


Fig. 1. The brain from which the data set was taken. The region of interest for the serial histological data acquisition is outlined with the dotted line.

St-Jean et al., 1998; Xu and Nowinski, 2001). Diffusion tensor imaging has also been used to map thalamo-cortical connections in order to derive probabilistic segmentations of the human thalamic nuclei (Behrens et al., 2003; Johansen-Berg et al., 2005). However, at this time, neither of these *in vivo* imaging techniques is able to provide the resolution required to accurately identify the subcortical nuclei targeted in functional neurosurgery, and therefore cannot provide the detailed segmentation that we present here.

Print atlases were the first visualization tools used to aid in the identification of anatomical structures for surgical planning (Afshar et al., 1978; Ono et al., 1990; Schaltenbrand and Bailey, 1959; Schaltenbrand and Wahren, 1977; Schnitzlein and Murtagh, 1980; Talairach and Tournoux, 1988, 1993; Van Buren and Borke, 1972; Watkins, 1969). Typically, digital atlases are 3D visualizations of the data presented in these atlases. When digital atlases were first used, linear transformations matching the atlas to patient data were used to register an atlas to an individual patient scan (Bertrand et al., 1973; Nowinski et al., 1997; Otsuki et al., 1994). Our group was one of the first to estimate and apply nonlinear transformations to warp a digital atlas to fit pre-operative patient MR data in order to account for local variations in the anatomy (St-Jean et al., 1998).

A number of digital atlases of the human brain, based on print atlases, have been previously published. Nowinski et al. (1997) have developed an integrated digital atlas that incorporated data from three print atlases by Ono et al. (1990), Schaltenbrand and Wahren (1977), and Talairach and Tournoux (1988). All three atlases are registered together using landmark based linear transformations needed to map the Ono et al. (1990) and Schaltenbrand and Wahren (1977) atlases into Talairach space (Talairach and Tournoux, 1988). In order to register the combined atlas to a subject or patient, a piece-wise linear approach is used to transform the atlas to the MR volume. The Talairach and Tournoux atlas was also used as the foundation for a digital atlas by Ganser et al. (2004). The original plates were scanned and reconstructed in three dimensions by calculating a Delauney tetrahedrization. The surfaces of anatomic structures in the Talairach atlas were reconstructed using the marching cubes algorithm (Lorensen and Cline, 1987). The resulting volume was then intersected at half the slice-to-slice distance to complete the interpolation.

The digital atlas used previously at the Montreal Neurological Institute (MNI) was developed by St-Jean et al. (St-Jean et al., 1998). It is based on a 3D reconstruction of the axial contour data from the Schaltenbrand and Wahren atlas (Schaltenbrand and Wahren, 1977). The digital atlas included 16 structures and has a varying slice thickness of 0.5 to 3mm due to the slice-to-slice

distance of the original atlas. The reconstructed data set was interpolated with a Hermite polynomial (Foley et al., 1990) to achieve a 0.5mm isotropic resolution. Slice-to-slice spatial inconsistencies in structure contours were considered to be small, and thus not accounted for. The interpolated digital atlas was warped in 3D to fit a high resolution, high signal-to-noise ratio standard reference volume that is the result of the average of 27 MRI scans of the same subject (Holmes et al., 1998), known as the Colin27 MRI average. The warping was achieved via a thin-plate-spline (TPS) (Bookstein, 1989) transformation based on 250 homologous landmarks manually identified by a neuroanatomist on both volumes. The result is a set of anatomical labels defined in the region of the basal ganglia and thalamus that are aligned with the Colin27 MRI average. In order to customize the digital atlas to patient MRI data, a nonlinear transform between the Colin27 MRI average and a patient's MRI is estimated automatically (Collins and Evans, 1997; Collins et al., 1995). This transformation is applied to the digital atlas to map it onto patient's pre-operative MRI to facilitate surgical planning.

While this atlas has proven very useful (Atkinson et al., 2002; Duerden et al., 2003), it has limited inherent resolution in the slice direction (0.5 mm), contains a limited number of structures, and contains some small misregistrations between the digital atlas and the Colin27 MRI average that are propagated to patient MRI data during the atlas customization procedure.

In this manuscript, these limitations are addressed. Techniques are developed for the creation of a new and improved atlas for stereotactic neurosurgery. This atlas contains both histological and geometric (i.e., structural anatomical) data and is registered to a MRI reference volume. Preliminary work on this new atlas was presented in (Chakravarty et al., 2003). The new digital atlas is derived from a single set of high-resolution, thin-slice histological data of the region of basal ganglia and thalamus. The atlas contains 105 anatomical structures that were manually delineated by a neuroanatomical expert on the histological data using sources for the gross anatomy (Schaltenbrand and Wahren, 1977), for the temporal lobe (Gloor,

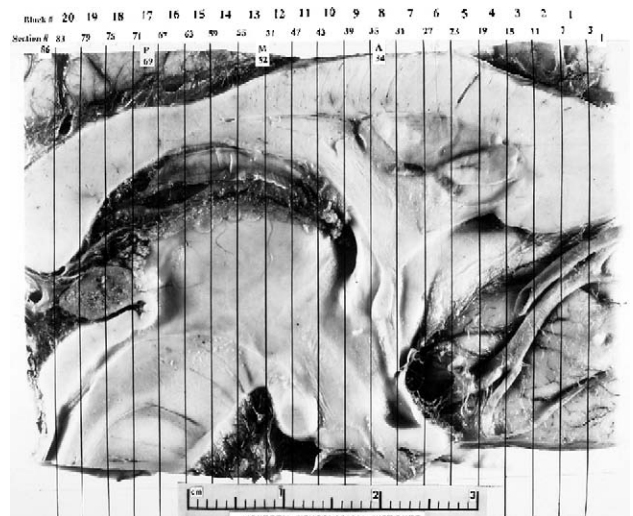


Fig. 2. Close-up of the region of interest shown in Fig. 1. Between each pair of vertical lines, four nissl- and myelin-stained slices were acquired. Adjacent pairs of nissl- and myelin-stained slices were photographed and overlaid on top of one another to create a single slice used in this dataset. Examples of the 2D histological data used to create a 3D histological volume are shown in Fig. 3.

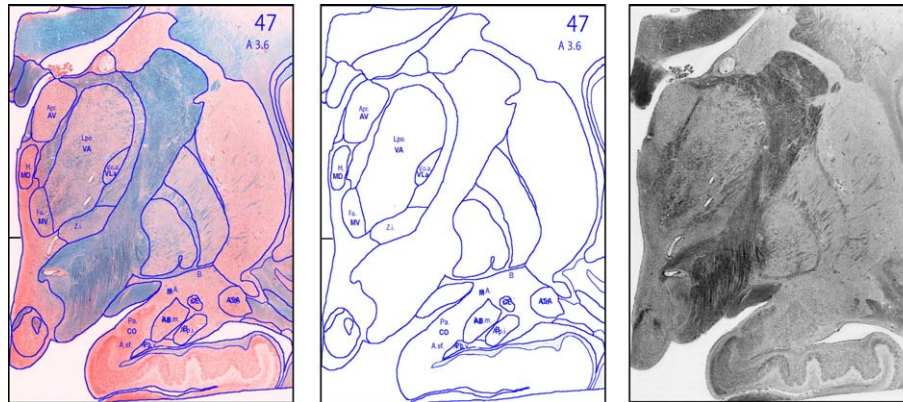


Fig. 3. An example of the data set: a coronal slice through the center of the volume. Slices show the nuclei of the thalamus, caudate nucleus, putamen, globus pallidus, claustrum as well as the myelinated fibers of the internal capsule, corpus collosum, external capsule, and the extreme capsule. Left: the color data with segmentation lines drawn. Middle: the segmented contours. Right: grey-level image.

1997) and for the thalamus (Hirai and Jones, 1989). The histology was parceled three times according to these sources. To reconstruct the histological and geometric data in three dimensions (3D), the structure contours were used in the development of an optimization procedure for slice-to-slice registration and intensity correction of the histological data. These reconstructions were registered to the Colin27 high resolution reference MRI (Holmes et al., 1998), using a novel atlas-to-MRI matching technique. Atlas customization (to any subject scan) can be achieved through a flexible nonlinear atlas-to-subject registration technique.

Our long-term goal is to use this refined atlas to improve pre-operative planning and thereby positively affect the outcome for patients undergoing surgeries for movement disorders. Since this atlas contains a detailed segmentation and classification of subcortical nuclei, it can also be used in post-operative follow-up and in other applications requiring a detailed analysis of the basal ganglia and thalamus.

In this paper, we will discuss the optimization of a slice-to-slice histological data registration technique (Chakravarty et al., 2003) used to minimize morphological misalignment throughout the histological volume. The parameters are optimized based on the minimization of error between the segmented contours of seven pairs of adjacent slices which span the dataset. These parameters are then used to register all consecutive pairs of slices of the histological data. In addition, an improved intensity inhomogeneity correction technique based on previous work (Chakravarty et al., 2003), the creation of a 3D geometric atlas, and an atlas-to-template warping technique are also presented. Since the reconstruction and intensity correction of histological data plays an integral role in this work, the next section will review previous techniques used in these domains.

Previous work: the 3D reconstruction of histological data

The atlas presented in this paper is based on a 3D histological reconstruction technique which was developed for the reconstruction of a fully labeled set of histological data. Serial histological data sets are notoriously difficult to reconstruct due to the unpredictable nature of the artefacts introduced when the brain is sectioned in a microtome. Such artefacts include tearing, stretching, and compression. Intensity inhomogeneities can also occur due to inhomogeneous staining densities and inconsistent lighting.

Groups studying the reconstruction of histological data typically employ one or more of the following steps:

- (1) Slice-to-slice registration techniques to minimize structural inhomogeneities between slices.
- (2) Slice-to-blockface registration to further minimize the structural inhomogeneities of a single slice. We define the blockface to be the photograph of the volume prior to the acquisition of a single slice histological data. The blockface serves as a local reference for the single slice.
- (3) Reconstructed volume to global reference warping to deal with global structural inhomogeneities. Global references may include Magnetic Resonance Imaging (MRI), Computed Tomography (CT) or Positron Emission Tomography (PET) data.

This section will briefly review methods used for the reconstruction and intensity correction of histological data.

A group dealing with the analysis of signal changes found in the MR volumes acquired from patients suffering from Creutzfeldt–Jakob disease developed novel techniques to reconstruct photographs from the anterior and posterior surfaces of thickly sliced (12 mm) cryogenic data (Bardinet et al., 2003; Colchester et al., 2000). Two different transformations are estimated. In the first, a landmark-based rigid-body transformation is used on each individual slice to register the anterior and posterior side photographs. In the second, a block-matching strategy (Ourselin et al., 2001) is used to estimate a rigid transformation between the anterior side and the block-face of the cryogenic volume. The 3D reconstructed histological volume was then registered to an MR volume of the same brain using an iterative closest point (ICP) technique. These methods were later improved by Kenwright et al. (2003) by using an ICP technique to first register the outer brain surfaces of the histological volume and

Table 1
Parameters used in the registration procedure for different resolutions in scale space

	Step 1	Step 2	Step 3
FWHM (μm)	640	340	200
Step size (μm)	1700	850	510
Lattice diameter (μm)	3400	1700	1020
Sub lattice	30	20	20

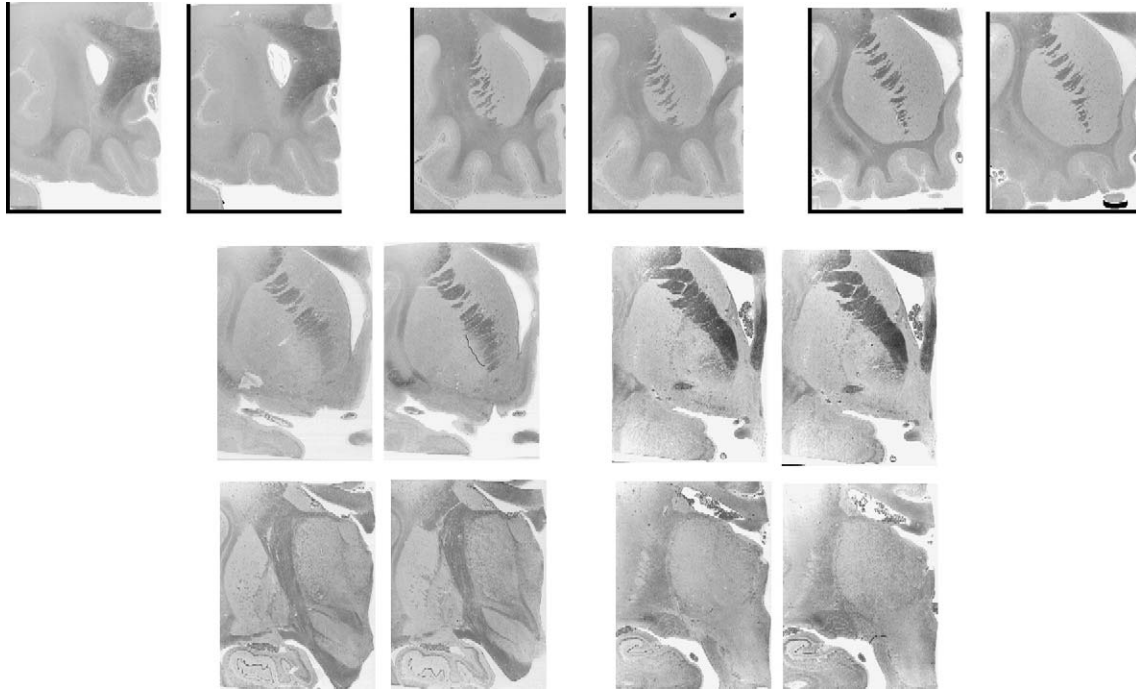


Fig. 4. Data used for parameter optimization of ANIMAL. Seven pairs of adjacent slices were taken from the volume. Slices from different areas of the brain will have different shape and intensities due to varying amounts of grey and white matter in each slice. These slices were selected get a representative sample from the entire data set in order to estimate the optimal stiffness, weight, and similarity values to use in the registration process.

the MR volume. This transformation was then refined by registering each individual slice within the MR volume.

Malandain et al. (2004) performed the 3D reconstruction of 2D autoradiographs of a rhesus monkey in order correlate histology with functional activity found in the awake monkeys during an fMRI scan. The data used do not have any photographic block face reference, but an MRI volume is used as a global reference. The 3D reconstruction uses the block matching strategy of Ourselin (Ourselin et al., 2001) mentioned in the previously. An initial set of 3D subsections is created. A slice in each subsection is chosen as a reference to which the remaining slices in the subsection are registered using a rigid body transformation. Each of these subsections is then registered to a single reference section in order to create a 3D volume. A slice-by-slice intensity correction scheme which uses an affine transformation to match the histograms of each slice to a single reference slice is employed. A refinement of this initial reconstruction is done using a slice-by-slice correspondence established with the reference MR. Only 2D affine slice-to-MRI transformations are used so no slice is interpolated out of the autoradiograph slice-acquisition plane.

Schormann and Zilles (1998) developed a technique for the reconstruction of serial histological data, which was later used in a population study of the position and spatial variability of the optic radiations (Burgel et al., 1999) and the human motor system

(Rademacher et al., 2001). Slices of histological data are digitized using a camera and individual slices were registered to a single slice in the dataset using linear rigid-body transformation estimated using a least-squares technique. Each slice is then registered with the corresponding video block face using a linear transformation estimated using a modified version of the principal-axes transformation (PAT) which accounts for shearing in the slice plane that the regular PAT does not (Schormann and Zilles, 1997), and a 2D nonlinear transformation. The resulting reconstructed volume was modeled as an elastic medium which was registered to an MRI reference using a nonlinear deformation estimated from the solution of a system of partial differential equations subject to the mechanical constraints of the medium.

Other groups have used landmark based techniques to reconstruct serial histological data. Toga et al. (1997) used a fiducial marker based registration process to align serial sections of cryogenic data. Their method uses a combination of local and differential scaling to put the anatomical data in Talairach space (Talairach and Tournoux, 1988). Kim et al. (1997) used a TPS (Bookstein, 1989) technique to reconstruct a set of rat brain autoradiographs to a video block face reference. Their technique was implemented using landmarks which are automatically defined on a grid or circle, and these landmarks move during each iteration so that the transformation seeks to minimize the mutual information between the images after warping.

Table 2

Region of the parameter space resampled to determine optimal transformation

FWHM (μm)	Similarity (t_1)	Stiffness (t_2)	Weight (t_3)
640	$0.65 \leq t_1 \leq 0.95$	$0.35 \leq t_2 \leq 1$	$0.85 \leq t_3 \leq 1.5$
340	$0.65 \leq t_1 \leq 0.95$	$0.35 \leq t_2 \leq 1$	$0.75 \leq t_3 \leq 1.5$
200	$0.75 \leq t_1 \leq 0.95$	$0.15 \leq t_2 \leq 1$	$0.05 \leq t_3 \leq 0.45$

Table 3

Optimized parameters found for similarity, stiffness, and weight for each resolution used in the outer loop

FWHM (μm)	Similarity (t_1)	Stiffness (t_2)	Weight (t_3)
640	0.95	0.6	1.3
340	0.9	0.6	1.3
200	0.9	0.2	0.5

Techniques which rely on image features have also been developed. A histological volume for atlas-based target identification in deep brain surgical stimulation for patients suffering from Parkinson's disease was developed by Ourselin et al. (2001). Their reconstruction is based on a block-matching (Ourselin et al., 2000) strategy to calculate local affine transformations to minimize the effects of the slice-to-slice structural inhomogeneities. The reconstructed histological volume is registered to MR data of the same subject via a 3D version of the same block-matching registration strategy. Volumes from PET were used as references for histological reconstruction by Mega et al. (1997). First, histologically stained images are registered to a cryogenic block-face using a 3D elastic warping technique (Thompson and Toga, 1996). A region of interest analysis between the reconstructed histological volume and PET data yielded a method of correlating the two different modalities. Delzescaux et al. (2003) registered histological images of a baboon brain to an MR reference using a free-form deformation based on the optimization of mutual information, to estimate a deformation to map the histological volume to MRI volume of the same brain.

The correction of local intensities variations in histological data has not received much attention, but global slice-to-slice intensity correction via histogram matching has been addressed by Malandain et al. (Malandain and Bardin, 2003; Malandain et al., 2004). Daguét et al. (2004) also perform a histogram matching, where ranges of intensities representing a specific tissue class (grey matter, white matter, or basal ganglia) are matched on a slice-to-slice basis.

The reconstruction technique presented here does not rely on anatomical references (such as MR volumes or video information of the block-face) to correct for local and global structural inhomogeneities, due to the age of the serial histological data. A slice-to-slice nonlinear registration technique which minimizes anatomic mis-registration throughout the reconstructed data set is presented here. An intensity correction scheme is also presented which analyzes local neighborhoods on each slice in order to build a voxel-by-voxel multiplicative field to correct for local variations in image intensities between slices.

Histological data acquisition

The brain used to create this histological data set was acquired in 1957 from a male patient who died of non-neurological causes at the Montreal Neurological Institute/Hospital. This data set was chosen because it has been intensively studied and used for teaching over the past 45 years. In addition, it has been manually segmented over the course of 2 years and revised over the past 3 years.

The specimen was fixed in 10% formalin. After fixation, the brain was split along the midline with the left half of the septum pellucidum intact. The aqueduct of Sylvius was also divided through the length of the midline. From this left hemisphere, a rectangular block of tissue was cut with its superior and inferior surfaces parallel to the inter-commissural plane and the anterior, posterior, medial, and lateral surfaces perpendicular to the inter-commissural plane.

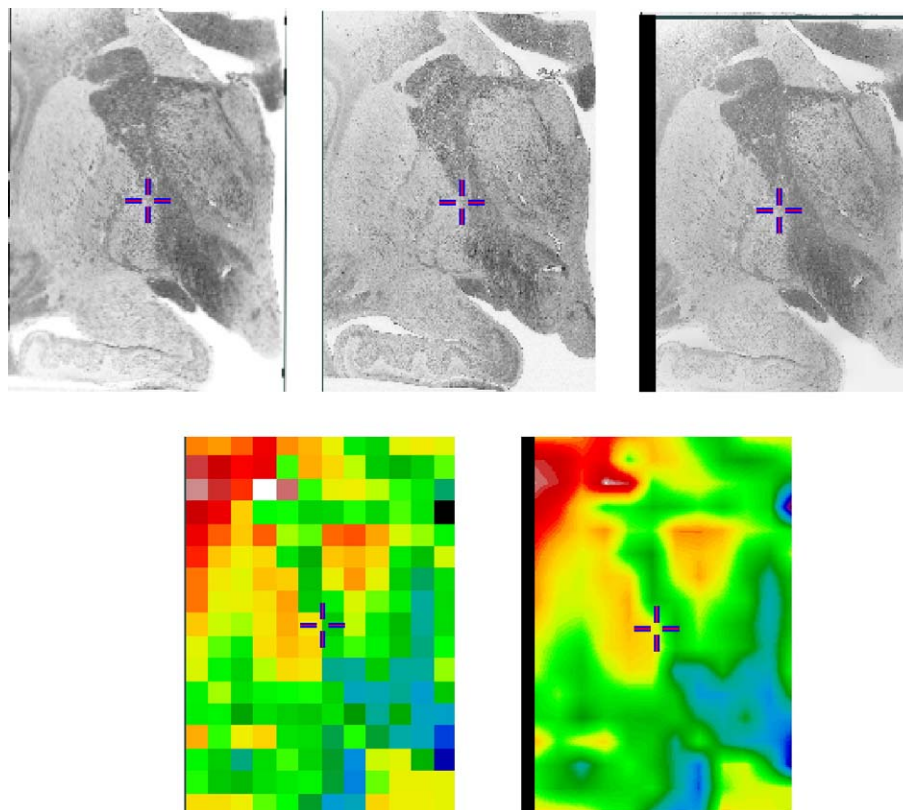


Fig. 5. Intensity correction. Top, from left to right: the original source image, the target image, the corrected image. Bottom, from left to right: estimated grid with intensity correction values stored in a neighborhood, the intensity correction grid resampled to match the voxel size of the original image. Cool colors represent lower scaling factors whereas hot colors represent higher scaling factors. Note that the intensity correction procedure described in this paper is estimated and averaged with both the previous and next slice in the series.

The superior portion of this block lies tangent to the upper-most portion of the corpus collosum and includes some of the cingulate cortex at the anterior and posterior ends of the block. The inferior plane of the block is at the level of infundibulum. The anterior most frontal section is a few millimeters behind the tip of the genu of the corpus collosum and the posterior most section is cut through the posterior end of the splenium of the corpus collosum and the very posterior aspect of the quadrigeminal plate. On the fixed brain, this block measured approximately 6 cm from front to back, 4.4cm from top to bottom, and 3.2 cm from side to side. This volume contains all of the thalamus, hypothalamus, and basal ganglia together with the amygdala and the hippocampus (except for the posterior portion). The original brain with the region of interest marked is shown in Fig. 1. A close-up of the region of interest is shown in Fig. 2.

After fixation, the block was mounted in paraffin prior to being microtomed into coronal sections. Pairs of slices were sampled from this data set at 0.70 mm intervals, yielding a total of 86 pairs of slices across the block. For each pair of slices, one was stained with Luxol Blue for myelin while the other was stained with a Nissl stain for cell bodies. Each slice was then photographed in black and white and the positive of each image was digitized using a flatbed scanner. Corresponding myelin and cell body photographs were overlaid on top of one another and the anatomy of each image was manually matched. The resulting images were digitally colored in Adobe Photoshop in red and blue to represent details regarding the cell density as well as myelinated fiber tracts. These are the histological images that are used to build a 3D reconstructed volume. This data was manually segmented by one of the authors (GB) using Adobe Photoshop. Each image has a center-to-center voxel spacing of $0.034 \text{ mm} \times 0.034 \text{ mm}$ and a slice-to-slice spacing of 0.7 mm. The

images were manually segmented and labeled combining information and nomenclature from three different references: for gross anatomy (Schaltenbrand and Wahren, 1977), the thalamus (Hirai and Jones, 1989), and the temporal lobe and the limbic system (Gloor, 1997). All of the labels, numbers and the anatomy associated with them are shown in Appendix A. The contours from this segmentation are used to build a geometric atlas.

For subsequent image processing, the contours were separated from the histological data layer. Both the histological and contour data were converted to grey-level images and used as input for the processing described in the next section. An example of the data set and the contours can be seen in Fig. 3.

3D reconstruction

As mentioned in the Introduction, artefacts are introduced into the data set during the acquisition of histological data. These may include, tearing, local compression, shearing, or stretching. If these slices of histological data are reconstructed (i.e., stacked) without any additional image processing steps, the resulting volume will be inhomogeneous with respect to intensity and morphometry in the slice direction (the so called “stack of pancakes” or the “banana reconstruction” problem (Malandain et al., 2004)). A nonlinear registration approach to reduce the effects of spatial artefacts in the data is presented in this section. Our preliminary work (Chakravarty et al., 2003) is improved here by optimizing different parameters used in the Automatic Nonlinear Image Matching and Anatomical Labeling (ANIMAL) (Collins and Evans, 1997; Collins, 1995) algorithm for slice-to-slice

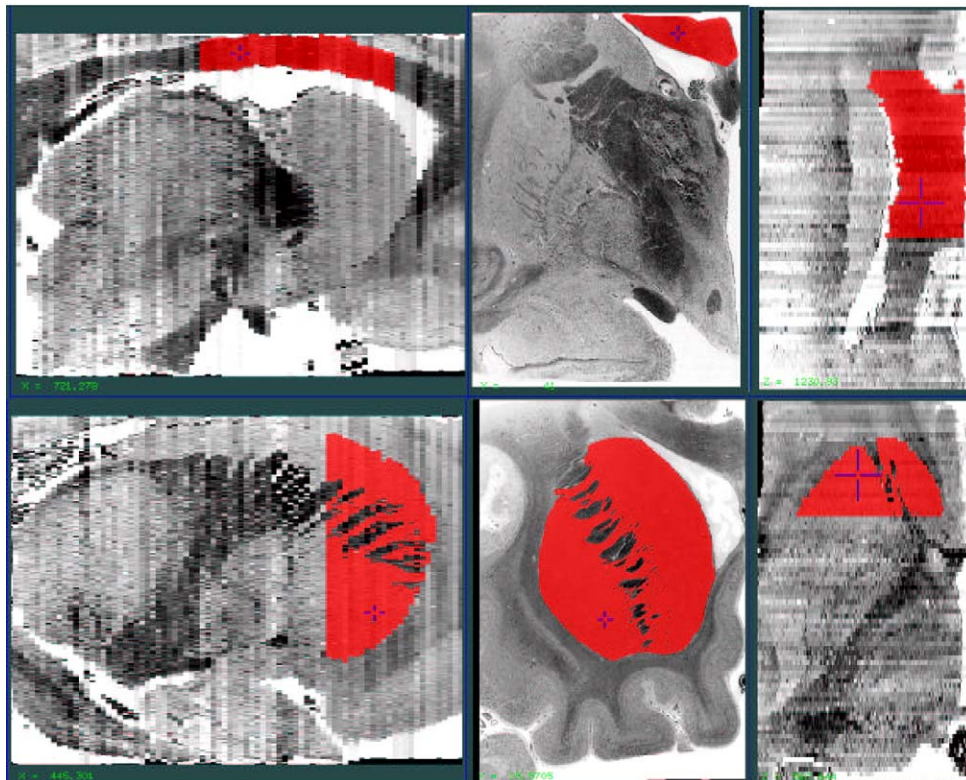


Fig. 6. ROIs defined for intensity correction optimization. Top: ROI for corpus collosum Bottom: ROI for striatum. ROIs shown are overlaid on histological volume before intensity correction.

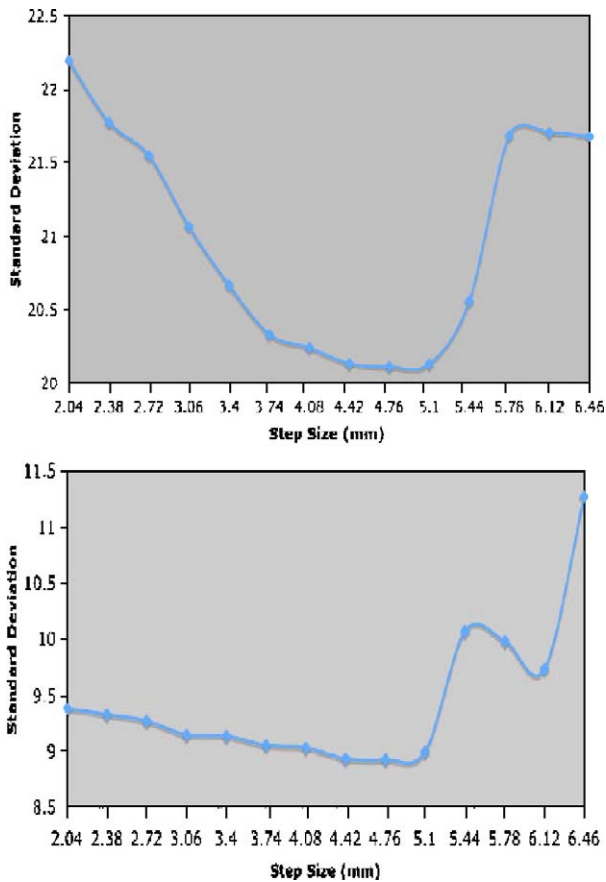


Fig. 7. Graphs of standard deviation versus changing step size for the ROI. Top: standard deviations for the striatum. Bottom: standard deviations for the corpus callosum. In both cases, the standard deviations for each slice is at a minimum at a step size of 4.76 mm.

registration of histological data. The following sections describe the ANIMAL algorithm and the parameter optimization procedure. The ANIMAL slice-to-slice registration procedure is applied to align all slices together to build a contiguous 3D histological volume in an algorithm described later.

Once a spatially contiguous 3D volume has been built, slice-to-slice intensity artefacts due to lighting and staining differences may remain. The intensity correction scheme presented here is an improvement over the global technique presented in (Chakravarty et al., 2003). Instead of computing a slice-by-slice global correction, the technique is modified to examine local changes in intensity on each slice in order to create a voxel-by-voxel scalar correction field. This intensity correction technique is also optimized in order to achieve the best intensity correction for the entire reconstructed volume. Details of this improved intensity inhomogeneity correction technique and the optimization of this technique are also provided.

ANIMAL and histological morphology correction

In the literature, slice-to-slice anatomical consistency is typically achieved by registration of the histological data to a reference image such as a block face (Bardinet et al., 2003; Colchester et al., 2000; Delzescaux et al., 2003; Kenwright et al., 2003; Kim et al., 1997; Ourselin et al., 2000; Toga et al., 1997). Since no reference data was

available for the histological data used here, the anatomical consistency between adjacent slices within the data set is maximized to achieve global three-dimensional consistency.

Nonlinear registration

Spatial inhomogeneities between successive slices are reduced by estimating a 2D deformation field to register two slices together. For each source–target pair of slices to be matched, ANIMAL defines a 2D regular lattice of control nodes. A vector is estimated at each node that maximizes the correlation ratio between the source and target data of the local intensity neighborhood centered at each lattice point. This similarity criterion is not sensitive to global intensity changes between slices. Only local changes in the contrast will affect the transformation estimation. This allows the computation of the spatial registration first, and the intensity correction afterwards. Bi-cubic interpolation is used to interpolate the deformation field between node points.

The nonlinear transformation is calculated in a hierarchical fashion, where large deformations are calculated on slices blurred with a Gaussian kernel with a large full-width at half-maximum (FWHM). The transformation estimated at a lower resolution is used as the input for the next step where it is refined by estimating a transformation on slices which have been blurred with a Gaussian kernel with a smaller FWHM. This procedure is repeated three times, and is known as the *outer loop*. At each step of the outer

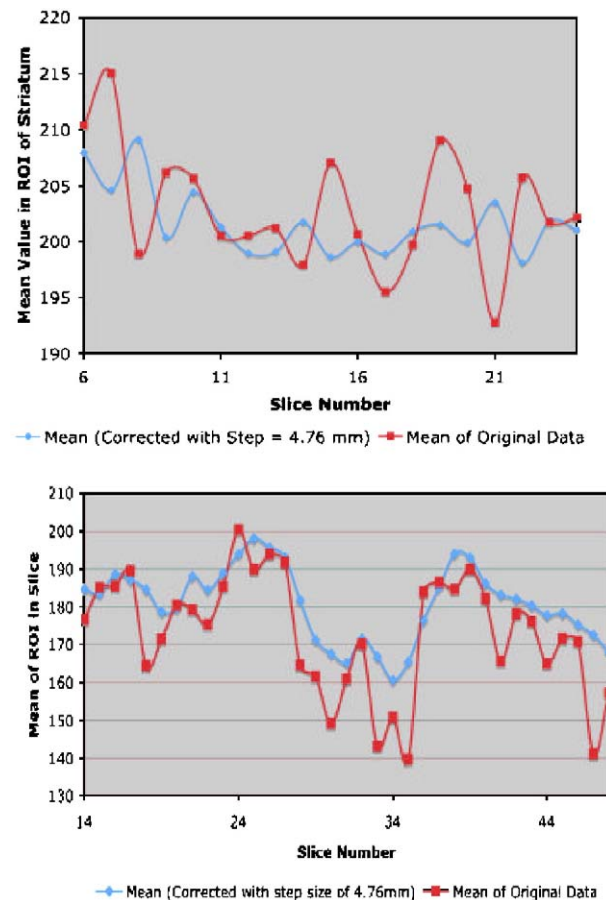


Fig. 8. Graph of the mean intensity on each slice in the ROI after the intensity correction process. Top: graph for striatum. Bottom: graph for corpus callosum. One can see that the slice-to-slice intensity varies much less after correction.

loop, the ANIMAL algorithm is applied iteratively in an *inner loop* to optimize the nonlinear transformation (N) that maximizes the similarity between a source slice (S) and a target slice (T) with the following objective function Γ :

$$\Gamma(S, T; N) = \beta(S, T; N) + C(N) \quad (1)$$

where β is the local similarity measure (i.e., the correlation ratio) and C is a cost function. The nonlinear transformation is represented by a deformation field that is iteratively calculated in a two step process: the first step involves the calculation of local translations for each node defined by the optimizing Eq. (1) and the second is a smoothing step to ensure that the deformation field is continuous and does not cause stretching, tearing, or overlap.

The transformation N is estimated by calculating local translations at each node of the lattice grid. The global optimization of Eq. (1) is achieved by the local optimization at each node. Three parameters can be set which can change the quality of the nonlinear transformation that is estimated in the inner loop: *the similarity cost ratio* (t_1), *the stiffness* (t_2), and *the weight* (t_3). If we let d_i be the local translation at a node then

$$\Gamma_i(d_i) = t_1\beta(S, T; n_i + d_i) + (1 - t_1)C(d_i). \quad (2)$$

β is the local similarity measure calculated at a node n_i , C is a cost function limiting the size of the translation vector, and t_1 is *the similarity-cost ratio* which balances the similarity measure and the cost function. The similarity cost ratio is constant for all n_i .

As mentioned earlier, the transformation being calculated should be smoothly varying and therefore should not induce infinite compression, allow the overlap of two distinct nodes, or induce tearing of the image. The deformation field is therefore regularized using the average of the translation vectors from the neighboring nodes:

$$d_i' = (1 - t_2)d_i + t_2\mathbf{M}_i, \quad (3)$$

where \mathbf{M}_i is the mean deformation vector calculated from the immediate neighborhood of node n_i , and t_2 is the *stiffness* parameter where $0 \leq t_2 \leq 1$. Large values for the stiffness parameter yield a smooth deformation field, at the expense of properly estimating very local translations. Smaller stiffness values

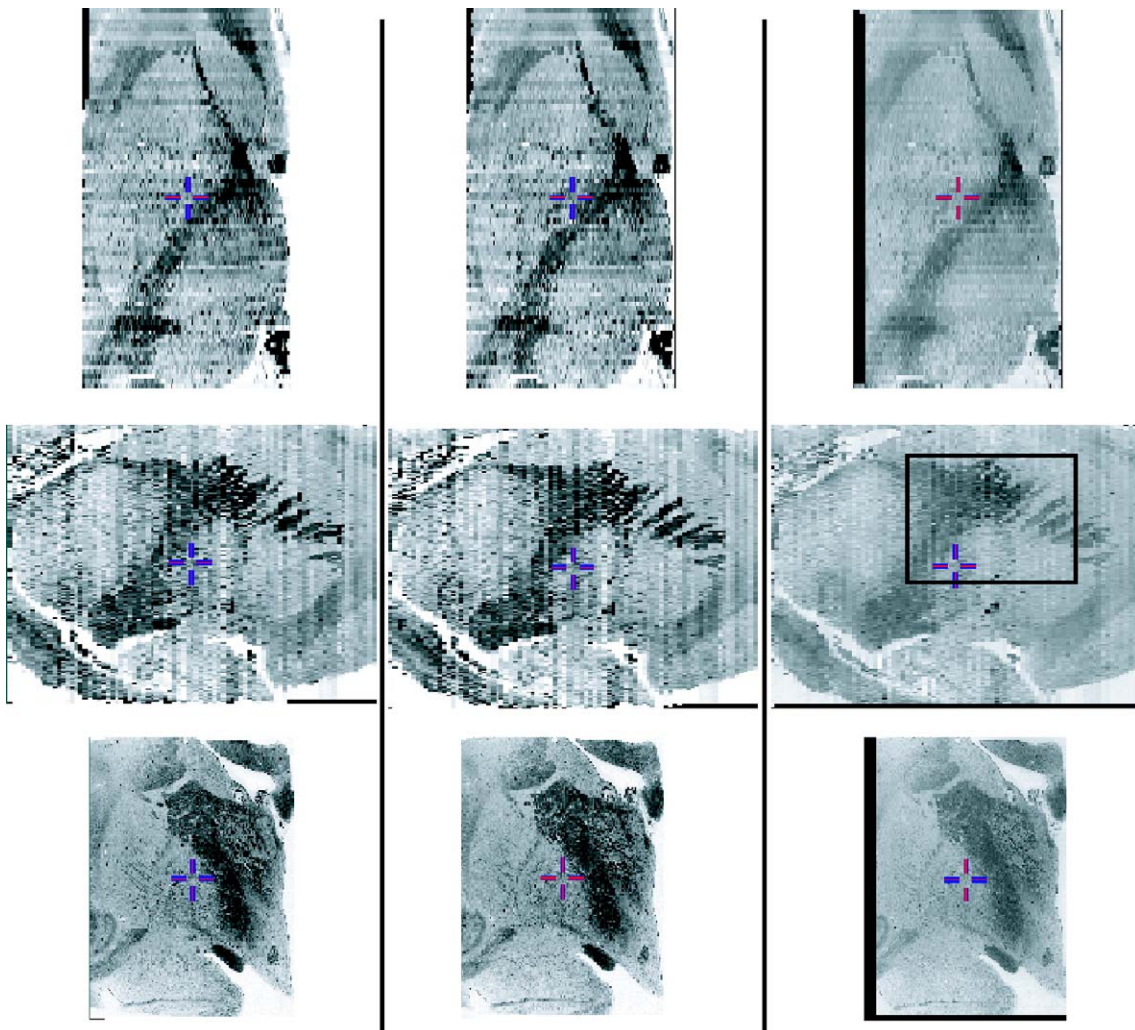


Fig. 9. Results of the 3D reconstruction. Left: reconstruction of the slices without any image processing steps (i.e., 2D images are simply stacked to form a volume). Middle: reconstruction of the slices after slice-to-slice registration. Right: reconstruction of the slices after intensity inhomogeneity correction.

will emphasize local translations, but the deformation runs the risk of being discontinuous.

ANIMAL builds an estimate of the nonlinear transformation over a fixed number of iterations for each resolution step (i.e., each step of the outer loop). At each iteration a fraction of each local translation estimate is added to the current iteration:

$$T(i) = t_3 d_i + T_{i-1} \quad (4)$$

where t_3 is a *weight* parameter for iterative update. The local translations are under-corrected if $t_3 < 1$ and are over corrected if $t_3 > 1$.

ANIMAL parameter optimization

The original parameters (t_1 , t_2 and t_3) for ANIMAL were optimized for registration of 3D MRI data. These parameters are re-optimized here for registration of 2D histological data. There are two differences between the procedure used here, compared to that of Robbins (Robbins et al., 2003). First, instead of minimizing entropy between two segmented MR volumes, 2D binary contour data is used with a distance function to evaluate the goodness of fit of the transformation estimated by ANIMAL. Second, the parameters are optimized independently for each step in the outer loop instead of globally.

The parameter optimization process was based on seven pairs of adjacent slices, selected throughout the data set to account for the changing anatomy over the volume of data (see Fig. 4). For each pair of slices one is assigned to be the source slice and the other slice to be the target. All three parameters were varied as follows: $0 < t_1 \leq 1$, $0 < t_2 \leq 1$, and $0 < t_3 \leq 1.5$ in 0.1 unit steps while the other registration parameters (see Table 1) remained constant. An exhaustive search strategy was used where a transformation was estimated for each combination of parameters

(1400 in all). The estimated transformation was then applied to the segmented contour data for each source image. The mean chamfer distance (Borgefors, 1984) between the transformed source contour data and the target contour data was recorded for each transformation over all pairs of slices (9800 distances maps) and used as the goodness of fit metric. The chamfer distance is an approximation the Euclidean distance function (Duda et al., 2000) which can be assessed on binary data where each non-contour pixel in each image is assigned a value which represents its distance from the closest contour.

The optimization was refined by supersampling the parameter space near the global minimum (i.e., within 5% of the minimum distance) with 0.05 unit steps as specified in Table 2. The optimization strategy described above was performed at each resolution in scale space (each step of the outer loop described in the section describing the ANIMAL algorithm for a total of 29400 transformations), yielding optimal parameters for similarity t_1 , stiffness t_2 and weight t_3 summarized in Table 3. The scale space parameters are the same as those outlined in Table 1.

3D reconstruction of 2D histological slices

Using the scale space technique described, each slice of the volume is registered twice; once to the adjacent slice previous to it in the series, and once to the next slice in the series. The optimized parameters found in the previous section were used to calculate each transformation. The average of these two transformations is applied to the original slice, such that the newly warped slice best matches its adjacent slices simultaneously. The registration procedure is given in Algorithm 1. It is important to note that the transformations are estimated for all slices in the dataset before they are applied to achieve the correction. The two transformations calculated will have

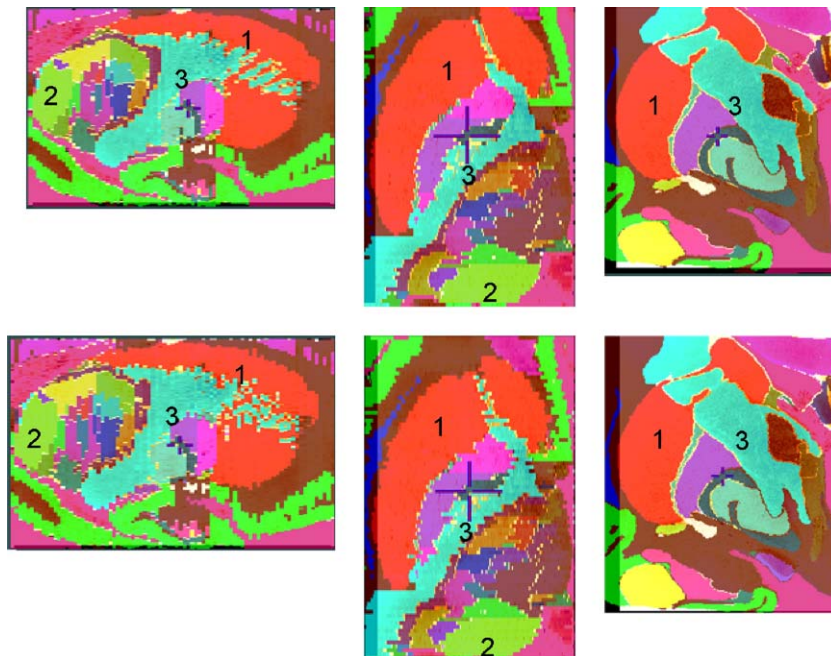


Fig. 10. Histological volume with voxel-label-atlas overlaid. Top: voxel-label data after the nonlinear transformations estimated have been applied to each slice. Bottom: voxel-label data before the nonlinear transformation has been applied to each slice in the dataset. Left: sagittal view. Middle: axial view. Right: coronal view. The results demonstrate how each structure is labeled by a unique color, and also how the structural borders have been smoothed after by the reconstruction described in 3D reconstruction of 2D histological slices. This is particularly evident in the striatum, particularly in the striations between the caudate nucleus and the putamen. Shown in all views are the 1. striatum, 2. internal capsule, and 3. pulvinar.

an additional function as they will also be used in the intensity correction procedure presented in the next section.

It should be noted here that this technique can only account for local deformations which exist between adjacent slices. Global deformations, such as overall shrinkage, cannot be accounted for using this slice-to-slice registration technique and will be addressed in the context of atlas-to-template warping.

Algorithm 1: Algorithm used to correct for spatial inhomogeneities

```

for slice = 1 to n do
  | set transformation[slice] to zero
for iter k = 1 to 3 do
  |
  | for slices i = 1 to n do
  | | blur[slicei with FWHMk]
  | | for slices i = 1 to n do
  | | |  $t_a[i, k]$  = estimate of deformation[slice  $i$  to slice  $i - 1$ ]
  | | | store  $t_a$  for intensity correction step
  | | |  $t_b[i, k]$  = estimate of deformation[slice  $i$  to slice  $i + 1$ ]
  | | | store  $t_b$  for intensity correction step
  | | | calculate intensity correction
  |
for slice = 1 to n do
  | set transformation[slice] = 0
  | update transformation[i] = average[ $t_a, t_b$ ]
  | apply transformation[i] to slice  $i$ 
  
```

Intensity inhomogeneity correction

Due to varying light intensity during photography, staining density, and slice thickness, the resulting histological volume will have varying intensities from slice-to-slice. For each slice, the hue and grey and white matter contrast were manually corrected using Adobe Photoshop by one of the authors (GB). These corrections were done in order to facilitate grey and white matter differentiation for structure identification on single slices. This correction does not correct for slice-to-slice differences throughout the volume. In the resulting 3D reconstruction of this volume, anatomical structures will not have homogeneous intensity values, visible as striping in the reconstructed slice directions. The limited work on the intensity correction of serial histological data (Chakravarty et al., 2003; Daguette et al., 2004; Malandain and Bardin, 2003) has considered global slice-to-slice intensity correction strategies. The intensity correction scheme developed here is a refinement of the global correction scheme presented in our previous work (Chakravarty et al., 2003) where a Least Trimmed Squares (LTS) fit (Rousseeuw and Leroy, 1987) was used to calculate a third order polynomial fit between the intensities of two different slices. Instead of a single global correction, our technique is modified here to account for local intensity inhomogeneity.

Intensity inhomogeneity correction algorithm

The intensity inhomogeneity algorithm minimizes the effects of intensity differences on the entire volume by correcting local intensity differences on each slice. We approach the slice-by-slice intensity correction of the histological data with a similar strategy as the morphological correction strategy presented earlier in this paper where the intensities in local neighborhoods on each slice are corrected by examining intensities in the same local neighborhood

on adjacent slices. Local differences in anatomy from slice-to-slice must be aligned to prevent the creation of intensity artefacts via local intensity correction estimates (as explained later in this section). To accomplish this alignment the final transformations estimated in the previous section are used to warp the adjacent slices of each slice. We then proceed to calculate a voxel-by-voxel correction grid for each slice.

After the warping, intensities are corrected in a two stage process described in Algorithm 2. The first is similar to our previous technique (Chakravarty et al., 2003) where the LTS fitting technique of Prima et al. (2001) was used to calculate two third order polynomials for each slice, where each polynomial maps intensities from a single slice to the slices adjacent to it. These polynomials are then averaged and applied to the single slice.

In the second step, local intensity variations are accounted for by estimation of a nonlinear correction field. Images are sectioned into square neighborhoods of equal size. We assume that if each square neighborhood is small enough, a first-order polynomial or scaling factor can be estimated mapping intensity values from a target neighborhood to a source neighborhood. For each neighborhood of slice i , two polynomials are estimated. One polynomial maps the intensities from the slice i to the corresponding neighborhood in slice $i - 1$, and the other to slice $i + 1$. The average of the two scaling factors is stored for each neighborhood center. After polynomials for all neighborhoods are estimated, an intensity correction field is interpolated using a bi-cubic kernel to match the resolution of the histological image. The original image is multiplied by the correction field to yield the corrected image. To demonstrate the application of the intensity correction between two images, Fig. 5 shows an example of an original image, a target image, the estimated field and the corrected image.

Algorithm 2: Algorithm used to correct for intensity inhomogeneities

```

for slice  $i = 1$  to  $n$  do
  |  $s_{i-1}$  = apply transformation  $t_{i-1}$  to slice  $i - 1$ 
  |  $s_{i+1}$  = apply transformation  $t_{i+1}$  to slice  $i + 1$ 
  |
  | for slice  $i = 1$  to  $n$  do
  | | define square neighborhoods of specified size on slice  $i, s_{i-1}$ , and  $s_{i+1}$ 
  | |  $g_{i-1}$  = estimate global correction using a third order LTS fit for [slice  $i$  to  $s_{i-1}$ ]
  | |  $g_{i+1}$  = estimate global correction using a third order LTS fit for [slice  $i$  to  $s_{i+1}$ ]
  | |  $g_i$  = average( $g_{i+1}, g_{i-1}$ )
  | | apply  $g_i$  to slice  $i$ 
  | |
  | | for all neighborhoods do
  | | |  $c_1$  = estimate correction factor using first order LTS fit for [slice  $i$  to  $s_{i-1}$ ]
  | | |  $c_2$  = estimate correction factor using first order LTS fit for [slice  $i$  to  $s_{i+1}$ ]
  | | | update scale factor for the neighborhood  $c$  = average( $c_1 + c_2$ )
  | | | update appropriate neighborhood in correction[slice]
  |
  | for slice  $i = 1$  to  $n$  do
  | | resample correction[slice] to match the resolution of slice  $i$ 
  | | multiply slice by the resampled correction[slice]
  
```

Optimization for step size

The step size for the intensity inhomogeneity correction was optimized to find the best value that would decrease the standard deviation of specific structure intensities. The effects of varying

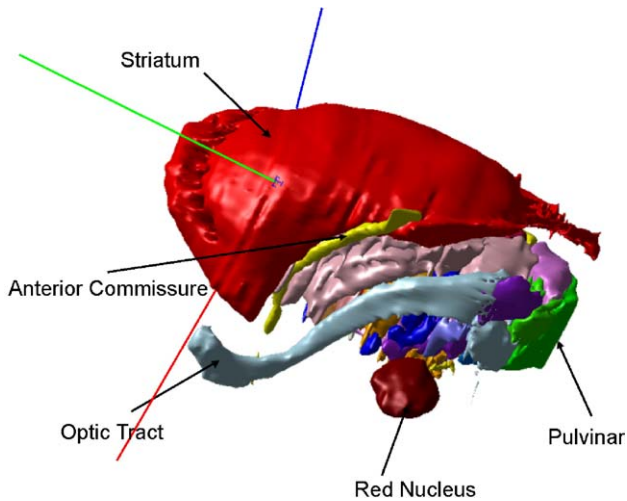


Fig. 11. 3D Geometric Atlas created from the voxel label data shown in Fig. 10. Structures identified are the striatum, anterior commissure, optic tract, red nucleus, and pulvinar (from a total of 105 structures in the atlas).

the step size were studied on two regions of interest (ROI). The ROIs selected were the striatum and the corpus colosum as they are relatively large structures which, in comparison to other anatomical structures in the brain, are expected to have relatively more uniform intensity throughout the histological volume (see Fig. 6). Intensity correction fields were estimated for each slice in the volume for step sizes from 2.04 to 6.46 mm, sampled at intervals of 0.34 mm. Step sizes lower than this range increase the computational burden of the correction process and step sizes above this range are too large to properly deal with the local natures of the intensity artefacts. The mean and standard deviation of intensity were computed in the region of interest for all voxels in the ROI. Since these regions are homogeneous, each one should have a similar mean value for all voxels. This is indicated by a minimal standard deviation value. Fig. 7 shows the standard deviation in the striatum and the corpus colosum as a function of changing step size. In both graphs, we see that a step size of 4.76 mm yields a minimum for the standard deviation. The standard deviation of intensities decreased 25% (from 11.84 to 8.4) in the corpus colosum and a 32% decrease in the striatum (from 29.59 to 20.11). Fig. 8 shows a plot of the mean intensity at each slice in the ROI before and after correction with a step size of 4.76 mm. This figure shows that the slice-to-slice intensity variation has been reduced.

Results and discussion of 3D reconstruction

The result of the 3D reconstruction can be seen in Fig. 9. The figure is organized as follows: The left panels show the reconstruction of the raw data, the middle panels show the reconstruction after undergoing the morphological correction, and the panel on the right show the reconstructions of the data after morphological correction and the intensity correction algorithms. The results demonstrate increased slice-to-slice continuity compared to a simple reconstruction of the data without any image processing steps. In the left and middle panels, while the overall structure can be seen in the reconstructed transverse and sagittal images, one can see banding in the anterior to posterior direction corresponding to differing slice-to-slice intensities. In the middle panels of Fig. 9, the sagittal and lateral views of the volume, we see a reduction in the local slice-to-slice misregistrations that are evident in the views of the left-most panel. Fig. 9 demonstrates how these local misregistrations, which are evident in the left panel, have been smoothed so that structural borders are now better defined. The right panels of the figure show a reduction in the slice-to-slice variation of intensities, and therefore better definitions of structural contours (see region identified in Fig. 9).

This initial reconstruction technique was devised to better define structures for histological data with no reference data. The volume must therefore be refined to account for any global deformations (such as shrinking or shearing) as well as other anatomical inaccuracies (as in the "stack of pancakes" or "banana reconstruction" problems). However, limitations of this technique (i.e., enforcing local consistency without any local block face or volumetric global references) can be accounted for by nonlinearly warping the atlas to the pre-operative MRI scans from a single patient, which is the subject of ongoing research (Chakravarty et al., 2005). This technique is introduced later in this article in the form of the warping of the atlas to an MRI template.

The slice-to-slice morphological and intensity correction techniques described rely on local measures to correct for global anatomical consistency. The validation of these techniques requires other fully segmented histological datasets to be reconstructed. It is likely that parameters (t_1 , t_{12} , and t_3 for morphological correction and step size for intensity correction) would require re-optimization for data which has been stained differently or from a different part of the brain using the optimization strategy presented here. Different types of data may require that the transformation be less stiff in order to allow larger local displacement of histological data which is more geometrically complex or have greater spatial distortion. The use of these datasets to validate these techniques

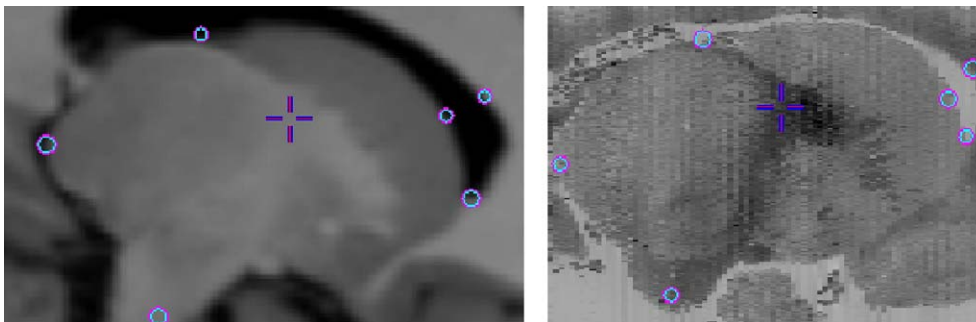


Fig. 12. Examples of histology-to-MR landmark definitions. Left: close up of the ROI in the reference-MR. Right: histological volume.

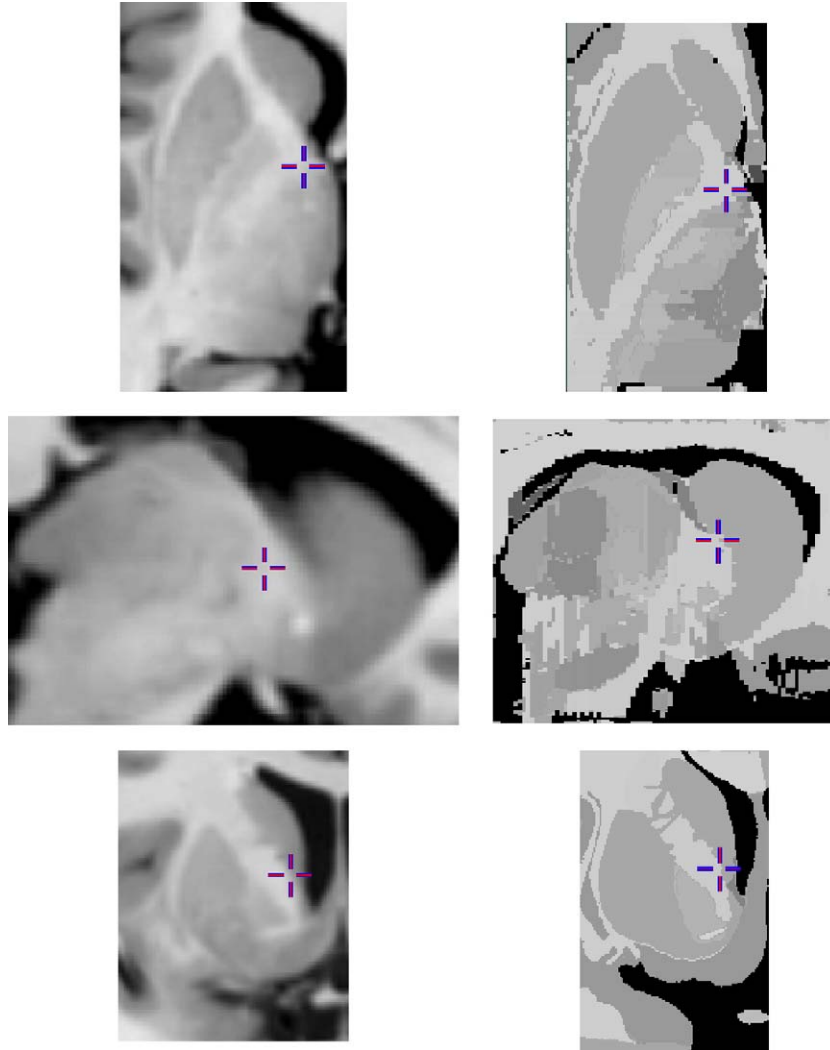


Fig. 13. Pseudo-MRI. Left: an average of 27 T1-weighted MR volumes taken from the same subject (the Colin27 MRI average). Close up into axial views of the basal ganglia and thalamus areas. Right: a pseudo-MRI created by matching replacing the voxel label values in Fig. 10 with intensity values from the MR-volume on the left.

is beyond the scope of this paper and will be the topic of further research.

Atlas of the basal ganglia and thalamus

The main goal of the atlas creation process is to develop a tool that will facilitate visualization and understanding of the 3D relationships of the structures that make up the basal ganglia and thalamus. This is achieved by building two atlas data sets from the contours manually defined on the original histological data. The first atlas is voxel-based, where structure labels are assigned to each voxel of the reconstructed histological volume. The *voxel label atlas* facilitates investigation of the histological volume when navigating through the transverse, sagittal or coronal slices of the volume. The second atlas is geometric, and enables visualization of the atlas structures in 3D from any viewpoint.

The process begins with the contour data defined on the original histological data as input to the generation of both atlases. In order to label all voxels of the histological volume, it was necessary to fill the regions defined by the contours with a unique label. Each

region was assigned an integer label (totaling 105 regions). Region filling was done with a simple 4-connected flood-fill algorithm (Duda et al., 2000) using manually placed seeds within each region. Leaks were manually fixed. When completed, each voxel of each histological slice was labeled with a structure identifier.

Since the structure region labels were defined on the original histological slice data, they suffer from the same slice-to-slice morphological inconsistencies. These spatial artefacts can be corrected by applying the averaged transformations estimated at each slice to each label in the dataset. Since both histological slice data and voxel labels are warped by the same transformation, structures and labels remain contiguous from slice-to-slice. The

Table 4
Parameters used to calculate atlas-to-subject transformation using ANIMAL

Step	Step size (mm)	Sub lattice diameter	Sub lattice
1	4	10	8
2	2	6	6
3	1	6	3

transformed label data from each slice are then stacked together to form a 3D voxel label atlas of the region of the basal ganglia and thalamus (see Fig. 10).

Generation of geometric structures from the voxel label atlas was completed using a modified version of the marching cubes algorithm (MacDonald, 1998) and can be seen as a set of 3D objects in Fig. 11.

Atlas to template warping

Our current atlas-to-patient warping technique (St-Jean et al., 1998) uses the Colin27 MRI average (Holmes et al., 1998) as an intermediate template for registration. To use the reconstructed histological volume, the voxel label atlas and the geometric atlas created here for surgical planning, they must be first aligned with the Colin27 MRI average.

A two step procedure is used to bring the atlas data into the same reference space as the Colin27 template. First, an affine transformation based on 24 homologous landmark-pairs (see Fig. 12) was estimated (Sibson, 1978) to roughly align the atlas and template volumes. The homologous landmark pairs were chosen on easily identifiable structures such as the striatum, thalamus, and the lateral ventricle. These points are required only to estimate an initial affine transformation between the atlas and the Colin27 MRI reference. As mentioned in the results and discussion section, this initial transformation is an estimate which accounts for the global deformations between the reconstructed volume and the Colin27-MRI average that the morphological correction algorithm cannot. However, this technique cannot recover the global deformations of the original dataset, as no original global reference exists.

In the second step of this procedure, the atlas is warped using the ANIMAL nonlinear registration strategy to account for the remaining morphological differences between the atlas and template. Since ANIMAL uses cross-correlation as a similarity criterion to compute local 3D translations, a pseudo-MRI was created from the voxel label atlas. Each of the structures in the voxel label atlas was manually assigned an intensity value from the

corresponding structure found in the Colin27 template. The result is a pseudo-MRI volume which has similar contrast to the Colin27 template MRI volume (see Fig. 13). The intensity values given to structures on the atlas to create the pseudo-MRI are limited to the structures which are also visible on the MRI template. Intensities for structures that were difficult to resolve on the template MRI but exist on the atlas were approximated based on the structure on both templates.

ANIMAL was applied using the parameters listed in Table 4 to estimate the transformation required to bring the pseudo-MRI into alignment with the Colin27 template. This deformation field was applied to all the atlas data to bring it into alignment with the Colin27 template and was estimated using a mask which allows ANIMAL to only estimate a transformation in the space in which the atlas exists.

Though not shown in this paper, this atlas needs only to be reflected about the midline of the Colin27 MRI average to exist on the right side. Local variability on the right side can be minimized by re-estimating a nonlinear transformation. Subject-to-subject anatomical variability can be accounted for using ANIMAL to estimate an atlas-to-subject nonlinear transformation. Different atlas-to-subject nonlinear warping techniques are currently being explored and are the subject of ongoing investigation (Chakravarty et al., 2005).

Fig. 14 shows sagittal and coronal views of the reconstructed histological volumes and the voxel label data warped to fit the Colin27 template. Fig. 15 shows the voxel label atlas and the geometric atlas, warped to fit the Colin27 template. These images demonstrate how the nonlinear warp accounts for local variations between the atlas and the reference-MR. In the bottom right of Fig. 15 the 3D geometric atlas is shown after being warped in the reference space of the reference-MR.

Conclusions and further research

This paper develops the steps used to create an atlas which can be customized to MR volumes. The process begins with serial

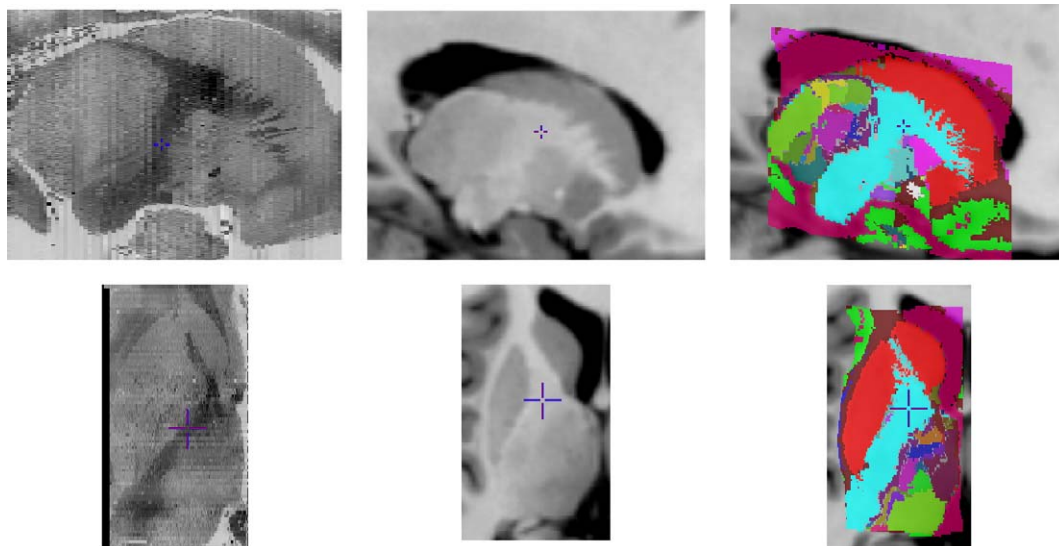


Fig. 14. Reconstructed histological volume and voxel label data warped to fit the Colin27 MRI average. From left to right: histological volume, colin27 MRI template, and the warped voxel label atlas overlaid on the Colin27 template. From top to bottom: sagittal and axial views.

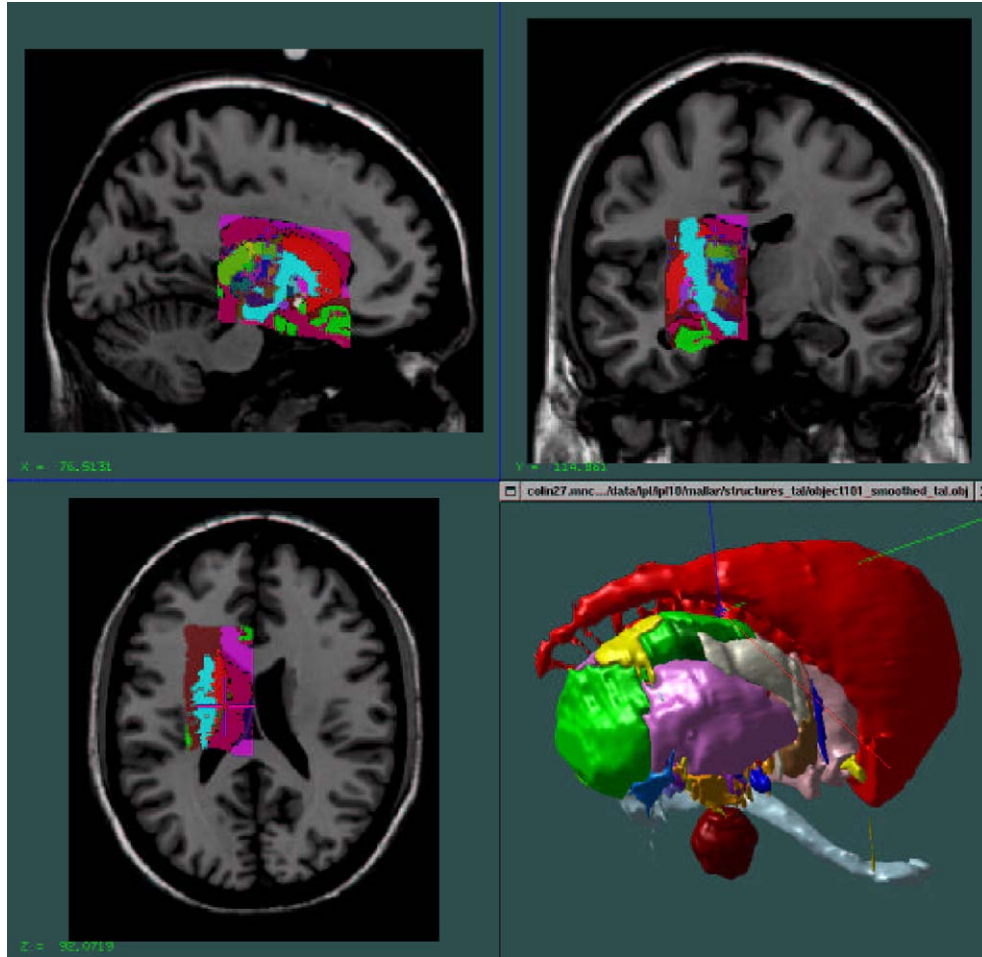


Fig. 15. Voxel label data warped to fit the Colin27 MRI average: the 3D Geometric Atlas is also warped to fit the reference MR and can be navigated with the tri-planar view.

histological data, stained with Luxol blue and Nissl stains. All of these slices are segmented manually to identify the basal ganglia and the thalamus. A histological volume was created using a nonlinear registration technique to greatly reduce the effect of artefacts that are introduced in the histological acquisition process. Optimal parameters were found to align histological slices using an error metric which compares the distance between segmented contours on adjacent slices. An improved intensity correction technique which analyzes local differences in intensity within the serial histological data set was used for a voxel-by-voxel intensity correction.

The transformations calculated for the histological data were applied to the manually identified contours to reduce the effects of slice-to-slice morphological variability. A new geometric atlas was created based on the tessellation of segmented contour data defined on the histological data.

An atlas customization technique, where a nonlinear transformation mapping this geometric atlas to a reference MR scan, was also presented. We will investigate a similar technique for atlas customization to patient scans. Since the atlas is based a single set of histological data from a single hemisphere, we must still determine if using nonlinear registration techniques will account for atlas-to-subject morphological variability. Future work includes the analysis of different atlas-to-subject registration processes, investigation of atlas-to-patient registration parameters and validation of the usefulness of this tool in the surgical planning

process. We are presently working on incorporating the new atlas data into our current image guided surgical planning software.

Appendix A. A list of anatomical structures

Appendix Table A1 give a complete list of anatomical structures available in the atlas.

Table A1
List of labels and anatomical structures

Label	Schaltenbrand and Wahren	Gloor	Hirai and Jones	Notes
1	striatum			
2	cortex			
3	claustrum			
4	internal capsule			
5	Globus Pallidus (Pm)			
6	Nucleus amygdalae profundus lateralis (A.p.l)	Lateral nucleus (L)		amygdala
7	Optic Tract (II)			
8	Nucleus amygdalae profundus intermedius (A.p.i)	Basal nucleus (B)		amygdala

Table A1 (continued)

Label	Schaltenbrand and Wahren	Gloor	Hirai and Jones	Notes
9	anterior commissure (Cm.a.)			
10	lateral medullary lamina (la.p.l)			
11	Globus Pallidus Internal (Pm.i)			
12	Globus Pallidus External (Pm.e)			
13	Anterior Perforated Substance (B)			
14	Nucleus amygdalae profundus lateralis (A.p.m)	Accessory Basal Nucleus (AB)		amygdala
15	Ventro-oralis internus (V.o.i.)			thalamus
16	Stratum septi pellucidi (Str.sep)			
17	Pro-thalamicus principalis centralis (Pth. Pr. Ce.)	bed nucleus of the stria terminalis (BNST)		hypothalamus
19	Nucleus facialis (VII)			
20	Nucleus amygdalae profundus ventralis (A.p.v)	Para Laminar nucleus (PL)		amygdala
21	Medial medullary lamina (la.p.m)			
22	Stria medullaris thalami (st. m)			
23	Nucleus paraventricularis hypothalami (Pv)			
24	Nucleus Reticulatus Polaris (Rt.po.)			
25	Zona incerta (Z.i.)			
26	Nucleus lateropolaris thalami (Lpo)		Ventral Anterior Nucleus (VA)	thalamus:see labels 36, 89, 90
27	Nucleus fasciculosus thalami (Fa)		Medioventral Nucleus (MV)	thalamus
28	Nucleus Anterior Principalis (Apr)		Nucleus Anteroventralis (AV)	thalamus
29	Mamillary body (M.m)			
35	Fornix (Fx)			
36	Dorso-oralis externus (D.o.e)		Ventral Anterior Nucleus (VA)	thalamus:see labels 26, 89, 90 for HJ
37	Nucleus Medialis (M)		Mediodorsal Nucleus (MD)	thalamus
39	subthalamic nucleus (Sth)			
40	Lamella medialis thalami (La. M.)			thalamus

Table A1 (continued)

Label	Schaltenbrand and Wahren	Gloor	Hirai and Jones	Notes
41	Campus Forellii (pars H2)			thalamus
47	pars compacta (Ni.c)/pars reticula (Ni.r)			substantia nigra
48	Ruber (Ru)			red nucleus
49	Nucleus Centralis (Ce.)		Central Median Nucleus (CM)	thalamus
51	Nucleus Parafascicularis (Pf.)			thalamus
52				WM in red Nucleus and travelling towards the thalamus
53	Nucleus Dorsalis superficialis (D.sf.)		Lateral dorsal Nucleus (LD)	thalamus
60	Fasciculus gracillis Goll (G)			
61	Praegeniculate (prG)			
63	Peduncle			
64	Nucleus peripedicularis (Ppd.)			thalamus
66	Ganglion habenulae medialis (H.m)			forms Hb with 67
67	Ganglion habenulae internus (H.i.)			forms Hb with 66
68	Corpus geniculatum mediale (G.m/G.Md)			
70	Nucleus Limitans (Li)		Posterior nucleus (Po)	thalamus
71	Ventro-caudalis parvocell (V.c.pc)		Basal ventral medial nucleus/ Ventral posterior inferior nucleus (VMb/VPI)	thalamus
73	Lemniscus medialis (L.m.)			
74	Brachium colliculi inferioris (B.co.i)			
75	Nucleus Vestibularis (VIII)			
76	Area triangularis Wernicke (A.tr.W)			
81	Ventro-oralis medialis (V.o.m.)		Ventral Medial Nucleus (VM)	thalamus
86	Ventro-oralis internus (V.o.i.)		Ventral Lateral Posterior Nucleus (VLp)	thalamus: see labels 86, 91, 92, 93, 94, 104, 111, 112, 114, 120 for HJ
87	Ventro-oralis anterior (V.o.a)		Ventral Lateral Anterior Nucleus (VLa)	thalamus: see labels 87, 88, 91, 123 for HJ
88	Ventro-oralis posterior (V.o.p.)		Ventral Lateral Anterior Nucleus (VLa)	thalamus: see labels 87, 88, 91, 123 for HJ

(continued on next page)

Table A1 (continued)

Label	Schaltenbrand and Wahren	Gloor	Hirai and Jones	Notes
89	Dorso-oralis internus (D.o.i)		Ventral Anterior Nucleus (VA)	thalamus: see labels 26, 36, 90 for HJ
90	Zentrolateralis oralis (Z.o.)		Ventral Anterior Nucleus (VA)	thalamus: see labels 87, 88, 91, 123 for HJ
91	Ventro-intermedius internus (V.im.i)		Ventral Lateral Posterior Nucleus (VLp)	thalamus: see labels 86, 91, 92, 93, 94, 104, 111, 112, 114, 120 for HJ
92	Zentro-lateralis externus (Z.im.e)		Ventral Lateral Posterior Nucleus (VLp)	thalamus: see labels 86, 91, 92, 93, 94, 104, 111, 112, 114, 120 for HJ
93	Zentro-intermedius internus (Z.im.i)		Ventral Lateral Posterior Nucleus (VLp)	thalamus: see labels 86, 91, 92, 93, 94, 104, 111, 112, 114, 120 for HJ
94	Ventro-intermedius externus (V.im.e)		Ventral Lateral Posterior Nucleus (VLp)	thalamus: see labels 86, 91, 92, 93, 94, 104, 111, 112, 114, 120 for HJ
95	Ventro-caudalis internus (V.c.i)		Ventral Posterior Medial Nucleus (VPM)	thalamus: see label 95, 113
96	Ventro-caudalis anterior internus (V.c.a.e)		Ventral Posterior Lateral Nucleus (VPLa)	thalamus: see labels 96, 97, 98 for HJ
97	Zentro caudalis externus (Z.c.e)		Ventral Posterior Lateral Nucleus (VPLa)	thalamus: see labels 96, 97, 98 for HJ
98	Zentro caudalis internus (Z.c.i)		Ventral Posterior Lateral Nucleus (VPLa)	thalamus: see labels 96, 97, 98 for HJ
99	Dorso-caudalis (D.c.)		Lateral Posterior Nucleus (LP)	thalamus: see labels 99, 100, 101
100	Nucleus pulvinaris orolateralis (Pu.o.l.)		Lateral Posterior Nucleus (LP)	thalamus: see labels 99, 100, 101
101	Nucleus pulvinaris oromedialis (Pu.o.m.)		Lateral Posterior Nucleus (LP)	thalamus: see labels 99, 100, 101
102	Ventro-caudalis portae (V.c.por)		Anterior Pulvinal Nucleus (Pla)	thalamus: see labels 102, 103

Table A1 (continued)

Label	Schaltenbrand and Wahren	Gloor	Hirai and Jones	Notes
103	Nucleus pulvinaris oroventralis (Pu.o.v)		Anterior Pulvinal Nucleus (Pla)	thalamus: see labels 102, 103
104	Nucleus ventrointermedius internus (V.im.i)		Ventral Lateral Posterior Nucleus (VLp)	thalamus: see labels 86, 91, 92, 93, 94, 104, 111, 112, 114, 120 for HJ
105	Nucleus pulvinaris intergeniculatus (Pu.ig)		Inferior Pulvinal Nucleus (Pli)	thalamus
106	Nucleus pulvinaris (Pu.m)		Medial Pulvinal Nucleus (Plm)	thalamus
107	Pulvinal laterale (Pu.l)		Lateral Pulvinal Nucleus (Pll)	thalamus
108	corpus collosum			
109	Cerebro-Spinal Fluid			
110	general white matter			
111	Dorso-intermedius internus (D.im.i)		Ventral Lateral Posterior Nucleus (VLp)	thalamus: see labels 86, 91, 92, 93, 94, 104, 111, 112, 114, 120 for HJ
112	Dorso-intermedius externus (D.im.e)		Ventral Lateral Posterior Nucleus (VLp)	thalamus: see labels 86, 91, 92, 93, 94, 104, 111, 112, 114, 120 for HJ
113	Ventro-caudalis anterior internus (V.c.a.i)		Ventral Posterior Medial Nucleus (VPM)	thalamus: see label 95, 113
114	Zentrolateralis intermedius (Z.im)		Ventral Lateral Posterior Nucleus (VLp)	thalamus
115	Ventro-caudalis externus (v.c.e)		Ventral Posterior Lateral Nucleus (VPLa)	thalamus: see labels 115, 118
116	Nucleus pulvinaris superficialis (Pu.sf)			thalamus
117	Ventro-caudalis parvocell externus (V.c.pc.e)		Ventral Posterior Inferior Nucleus (VPI)	thalamus
118	Ventro-caudalis posterior externus (V.c.p.e)		Ventral Posterior Lateral Nucleus (VPLa)	thalamus

(continued on next page)

Table A1 (continued)

Label	Schaltenbrand and Wahren	Gloor	Hirai and Jones	Notes
119	Pulvinar medialis (Pu.m)		Medial Pulvinar Nucleus (Plm)	thalamus
120	Ventro-oralis posterior (V.o.p)		Ventral Lateral Posterior Nucleus (VLp)	thalamus: see labels 86, 104, 120 for HJ
121	Zentro-intermedius externus (Z.im.e)		Ventral Lateral Anterior Nucleus (VLA)	thalamus
122	Ventro-intermedius externus (V.im.e)		Ventral Lateral Anterior Nucleus (VLA)	thalamus
123	Dorso-oralis internus (D.o.i)		Ventral Lateral Anterior Nucleus (VLA)	thalamus: see labels 87, 88, 91, 123 for HJ

References

- Afshar, E., Watkins, E.S., Yap, J.C., 1978. Stereotactic Atlas of the Human Brainstem and Cerebellar Nuclei. Raven Press, New York.
- Atkinson, J.D., Collins, D.L., Bertrand, G., Peters, T.M., Pike, G.B., Sadikot, A.F., 2002. Optimal location of thalamotomy lesions for tremor associated with Parkinson disease: a probabilistic analysis based on postoperative magnetic resonance imaging and integrated digital atlas. *J. Neurosurg.* 96 (5), 672–680. (October).
- Bardinet, E., Colchester, A.C.F., Roche, A., Zhu, Y., He, Y., Ourselin, S., Nailon, B., Hojjat, S.A., Ironside, J., Al-Sarraj, S., Ayache, N., Wardlaw, J., 2001. Registration of reconstructed post mortem optical data with MR scans of the same patient. In: Niessen, W., Viergever, M. (Eds.), Fourth International Conference on Medical Image Computing and Computer Assisted Intervention MICCAI 2003, Lecture Notes in Computer Science. Springer, Utrecht.
- Behrens, T.E.J., Johansen-Berg, H., Woolrich, M.W., Smith, S.M., Wheeler-Kingshott, C.A.M., Boulby, P.A., Barker, G.J., Sillery, E.L., Sheehan, K., Ciccarelli, O., Thompson, A.J., Brady, J.M., Matthews, P.M., 2003. Non-invasive mapping of connections between human thalamus and cortex using diffusion imaging. *Nat. Neurosci.* 6, 750–757.
- Bertrand, G., Olivier, A., Thompson, C.J., 1973. The computerized brain atlas: its use in stereotaxic surgery. *Trans. Am. Neurol. Ass.* 98, 233–237.
- Bookstein, F.L., 1989. Principal warps: thin-plate splines and the decomposition of deformations. *IEEE Trans. Pattern Anal. Mach. Intell.* 11 (6), 567–585.
- Borgefors, G., 1984. Distance transformations in arbitrary dimensions. *Comput. Vis. Graph. Image Process.* 27, 321–345.
- Burgel, U., Schormann, T., Schleicher, A., Zilles, K., 1999. Mapping of histologically identified long fiber tracts in human cerebral hemispheres to the MRI volume of a reference brain: position and spatial variability of the optic radiation. *NeuroImage* 10 (5), 489–499.
- Chakravarty, M.M., Bertrand, G., Descoteaux, M., Sadikot, A.F., Collins, D.L., 2003. The creation of a brain atlas for image guided neurosurgery using serial histological data. In: Ellis, R.E., Peters, T.M. (Eds.), Fifth International Conference on Medical Image Computing and Computer Assisted Intervention MICCAI 2003, Lecture Notes in Computer Science, Montreal, Canada. Springer, pp. 343–350. November.
- Chakravarty, M.M., Sadikot, A.F., Germann, J., Bertrand, G., Collins, D.L., 2005. Anatomical and electrophysiological validation of an atlas for neurosurgical planning. In: Duncan, J.S., Gerig, G. (Eds.), Seventh International Conference on Medical Image Computing and Computer Assisted Intervention MICCAI 2005, Lecture Notes in Computer Science, Palm Springs, USA, October, vol. 2. Springer, pp. 394–401.
- Cohn, M.C., Hudgins, P.A., Sheppard, S.K., Starr, P.A., Bakay, R.A.E., 1998. Pre- and postoperative evaluation of stereotactic pallidotomy. *Am. J. Neuroradiol.* 19 (6), 1075–1080 (June).
- Colchester, A.C.F., Ourselin, S., Zhu, Y., Bardinet, E., He, Y., Roche, A., Al-Sarraj, S., Ironside, J., Nailon, B., Ironside, J., Ayache, N., 2000. 3-d reconstruction of macroscopic optical brain slice images. In: Delp, Scott L., Digoia, Anthony M., Jarama, Branislav (Eds.), Medical Image Computing and Computer Assisted Intervention (MICCAI), Lecture Notes in Computer Science, Pittsburgh, USA. Springer, pp. 95–105. October.
- Collins, D.L., Evans, A.C., 1997. ANIMAL: validation and application of non-linear registration-based segmentation. *Int. J. Pattern Recogn. Artif. Intell.*, 1271–1294 (December).
- Collins, D.L., Holmes, C.J., Peters, T., Evans, A.C., 1995. Automatic 3-D model based neuroanatomical segmentation. *Hum. Brain Mapp.* 3, 190–208.
- Cuny, E., Guehl, D., Burbard, P., Gross, C., Dousset, V., Rougier, A., 2002. Lack of agreement between direct magnetic resonance imaging and statistical determination of a subthalamic target: the role of electrophysiological guidance. *J. Neurosurg.* 97 (3), 591–597.
- Dauguet, J., Mangin, J.F., Delzescaux, T., Frouin, V., 2004. Robust interslice intensity normalization using histogram scale-space analysis. In: Barillot, C., Haynor, D.R., Hellier, P. (Eds.), Medical Image Computing and Computer Assisted Intervention (MICCAI), Lecture Notes in Computer Science, Saint-Malo, France. Springer, pp. 242–249. September.
- Delzescaux, T., Dauguet, J., Condé, F., Maroy, R., Frouin, V., 2003. Using 3d non rigid fid-based method to register post mortem 3d histological data and in vivo MRI of a baboon brain. In: Ellis, R.E., Peters, T.M. (Eds.), Fifth International Conference on Medical Image Computing and Computer Assisted Intervention MICCAI 2003, Lecture Notes in Computer Science, Montreal, Canada. Springer. November.
- Deoni, S.C.L., Peters, T.M., Rutt, B.K., 2005. High resolution T1 and T2 mapping of the brain in clinically acceptable time with DESPOT1 and DESPOT2. *Magn. Reson. Med.* 53, 237–241.
- Duda, R.O., Hart, P.E., Stork, D.G., 2000. Pattern Classification, 2nd ed. John Wiley and Sons, New York, USA.
- Foley, D.L., van Dam, A., Feiner, S.K., Hughes, J.K., 1990. Computer Graphics, Principles, and Practice. Addison-Wesley, Reading, MA.
- Fujita, N., Tanaka, H., Takanashi, M., Hirabuki, N., Abe, K., Yoshimura, H., Nakamura, H., 2001. Lateral geniculate nucleus: anatomic and functional identification by use of MR imaging. *Am. J. Neuroradiol.* 22 (7), 1719–1726.
- Ganser, K.A., Dickhaus, H., Metzner, R., Wirtz, C.R., 2004. A deformable digital brain atlas system according to Talairach and Tournoux. *Med. Image. Anal.* 8 (1), 3–22.
- Gloor, P., 1997. The Temporal Lobe and The Limbic System. Oxford Univ. Press, New York.
- Gross, R.E., Lombardi, W.J., Lang, A.E., Duff, J., Hutchinson, W.D., Saint-Cyr, J.A., Tasker, R.R., Lozano, A.M., 1999. Relationship of lesion location to clinical outcome following microelectrode-guided pallidotomy for Parkinson's disease. *Brain* 122 (3), 405–416.
- Hirai, T., Jones, E.G., 1989. A new parcellation of the human thalamus on the basis of histochemical staining. *Brain Res. Brain Res. Rev.* 14 (1), 1–34.
- Holmes, C.J., Hoge, R., Collins, L., Woods, R., Toga, A.W., Evans, A.C., 1998. Enhancement of MR images using registration for signal averaging. *J. Comput. Assist. Tomogr.* 22 (2).
- Johansen-Berg, H., Behrens, T.E.J., Sillery, E., Ciccarelli, O., Thompson, A.J., Smith, S.M., Matthews, P.M., 2005. Functional-anatomical validation and individual of diffusion tractography-based segmentation of the human thalamus. *Cereb. Cortex* 15 (1), 31–39.
- Kenwright, C., Bardinet, É., Hojjat, S.A., Malandain, G., Ayache, N., Colchester, A.C.F., 2003. 2-d to 3-d refinement of post mortem optical

- and MRI co-registration. Fifth International Conference on Medical Image Computing and Computer Assisted Intervention MICCAI 2003, Lecture Notes in Computer Science, Montreal, Canada. Springer. November.
- Kim, B., Boes, J.L., Frey, K.A., Meyer, C.R., 1997. Mutual information for automated unwarping of rat brain autoradiographs. *NeuroImage* 5 (1), 31–40.
- Lenz, F.A., Normand, S.L., Kwan, H.C., Andrews, D., Rowland, L.H., Jones, M.W., Seike, M., Lin, Y.C., Tasker, R.R., Dostrovsky, J.O., Lenz, Y.E., 1995. Statistical prediction of the optimal site for thalamotomy in parkinsonian tremor. *Mov. Disord.* 10 (3), 318–328.
- Lombardi, W.J., Gross, R.E., Trepanier, L.L., Lang, A.E., Lozano, A.M., Saint-Cyr, J.A., 2000. Relationship of lesion location to cognitive outcome following microelectrode-guided pallidotomy for Parkinson's disease: support for the existence of cognitive circuits in the human pallidum. *Brain* 123 (4), 746–758.
- Lorensen, W.E., Cline, H.E., 1987. Marching cubes: a resolution 3d surface reconstruction algorithm. *Comput. Graph.* 21 (4), 163–169.
- MacDonald, D., 1998. A Method for Identifying Geometrically Simple Surfaces from Three Dimensional Images. PhD thesis, McGill University.
- Malandain, G., Bardinet, E., 2003. Intensity compensation within series of images. Fifth International Conference on Medical Image Computing and Computer Assisted Intervention MICCAI 2003, Lecture Notes in Computer Science, Montreal, Canada. Springer. November.
- Malandain, G., Bardinet, E., Nelissen, K., Vanduffel, W., 2004. Fusion of autoradiographs with an MR volume using 2-D and 3-D linear transformations. *NeuroImage* 23 (1), 111–127.
- Mega, M.S., Chen, S.S., Thompson, P.M., Woods, R.P., Karaca, T.J., Vinters, H.V., Small, G.W., Toga, A.W., 1997. Mapping histology to metabolism: coregistration of stained whole-brain sections to premortem PET in Alzheimer's disease. *NeuroImage* 5 (2), 147–153.
- Nowinski, W.L., Fang, A., Nguyen, B.T., Raphel, J.K., Jagannathan, L., Raghavan, R., 1997. Multiple brain atlas database and atlas based neuroimaging system. *Comput. Aided Surg.* 2, 42–66.
- Nowinski, G.L., Yang, W.L., Yeo, T.T., Bryan, R.N., Miller, G.A., 2000. Computer aided stereotactic functional neurosurgery enhanced by the use of the multiple brain atlas database. *IEEE Trans. Med. Imaging* 19 (1), 62–69 (January).
- Ono, M., Kubik, S., Abernathy, C.D., 1990. Atlas of the Cerebral Sulci. Georg Thieme Verlag/Thieme Medical Publishers, Stuttgart, Germany.
- Otsuki, T., Jokura, H., Takahashi, K., Ishikawa, S., Yoshimoto, T., Kimura, M., Yoshida, R., Miyazawa, T., (1994). Stereotactic gamma-thalamotomy with a computerized brain atlas: Technical case report. *Neurosurgery*, 35 (4), 764–768 (October).
- Ourselin, S., Roche, A., Prima, S., Ayache, N., 2000. Block matching: a general framework to improve robustness of rigid registration of medical images. In: Delp, S.L., DiGoia, A.M., Jaramaz, B. (Eds.), Third International Conference on Medical Image Computing and Computer-Assisted Intervention, MICCAI'2000, volume 1935 of Lecture Notes in Computer Science, Pittsburgh, USA. Springer, pp. 557–566. October.
- Ourselin, S., Bardinet, E., Dormont, D., Malandain, G., Roche, A., Ayache, N., Tandé, D., Parain, K., Yelnik, J., 2001. Fusion of histological sections and MR images: towards the construction of an atlas of the human basal ganglia. In: Niessen, W., Viergever, M. (Eds.), *Medical Image Computing and Computer-Assisted Intervention (MICCAI)*, Utrecht, Netherlands, pp. 743–751. October.
- Prima, S., Ayache, N., Barrick, T., Roberts, N., 2001. Maximum likelihood estimation of the bias field in MR brain images: investigating different modelings of the imaging process. In: Niessen, W.J., Viergever, M.A. (Eds.), Fourth International Conference on Medical Image Computing and Computer-Assisted Intervention, MICCAI'2001, volume 2208 of Lecture Notes in Computer Science, Utrecht, Netherlands. Springer, pp. 811–819. October.
- Rademacher, J., Burgel, U., Geyer, S., Schormann, T., Schleicher, A., Freund, H.J., Zilles, K., 2001. Variability and asymmetry in the human precentral motor system. A cytoarchitectonic and myeloarchitectonic brain mapping. *Brain* 124, 2232–2258.
- Robbins, S., Evans, A.C., Collins, D.L., Whitesides, S., 2003. Tuning and comparing spatial normalization methods. In: Ellis, R.E., Peters, T.M. (Eds.), Fifth International Conference on Medical Image Computing and Computer Assisted Intervention MICCAI 2003, Lecture Notes in Computer Science, Montreal, Canada. Springer. November.
- Rousseeuw, P.J., Leroy, A.M., 1987. *Robust Regression and Outlier Detection*. Wiley Ser. Probab. Math. Stat.
- Samuel, M., Caputo, E., Brooks, D.J., Schrag, A., Scaravilli, T., Branston, N.M., Rothwell, J.C., Marsden, C.D., Thomas, D.G.T., Lees, A.J., Quinn, N.P., 1998. A study of medial pallidotomy for Parkinson's disease: clinical outcome, MRI location and complications. *Brain* 121, 59–75.
- Schaltenbrand, G., Bailey, W., 1959. Atlas of Stereotaxy of the Human Brain. Georg Thieme Verlag, Stuttgart, Germany.
- Schaltenbrand, G., Wahren, W., 1977. Atlas for Stereotaxy of the Human Brain. Georg Thieme Verlag, Stuttgart, Germany.
- Schnitzlein, H.N., Murtagh, F.R., 1980. Imaging anatomy of the head and spine. A Photographic Color Atlas of MRI, CT, Gross, and Microscopic Anatomy in Axial, Coronal, and Sagittal Planes, 2nd ed. Urban and Schwarzenberg, Baltimore.
- Schormann, T., Zilles, K., 1997. Limitations of the principal-axes theory. *IEEE Trans. Med. Imaging* 16 (6), 942–947 (January).
- Schormann, T., Zilles, K., 1998. Three-dimensional linear and nonlinear transformations: an integration of light microscopical and MRI data. *Hum. Brain Mapp.* 6, 339–347.
- Sibson, R., 1978. Studies in the robustness of multidimensional scaling: procrustes statistics. *J.R. Stat. Soc.* 40, 234–238.
- St-Jean, P., Sadikot, A.F., Collins, L., Clonda, D., Kasrai, R., Evans, A.C., Peters, T.M., 1998. Automated atlas integration and interactive three-dimensional visualization tools for planning and guidance in functional neurosurgery. *IEEE Trans. Med. Imaging (TMI)* 17 (5), 672–680.
- Starr, P.A., Vitek, J.L., DeLong, M., Bakay, R.A., 1999. Magnetic resonance imaging-based stereotactic localization of the globus pallidus and subthalamic nucleus. *Neurosurgery* 44 (2), 303–314.
- Talairach, J., Tournoux, P., 1988. Co-Planar Stereotaxic Atlas of the Human Brain. Georg Thieme Verlag, Stuttgart, Germany.
- Talairach, J., Tournoux, P., 1993. Referentially Oriented Cerebral MRI Anatomy. Atlas of Stereotaxic Anatomical Correlations for Gray and White Matter. Georg Thieme Verlag, Stuttgart, Germany.
- Thompson, P.M., Toga, A.W., 1996. A surface-based technique for warping three dimensional images of the brain. *IEEE Trans. Med. Imaging* 15.
- Toga, A.W., Goldkorn, A., Ambach, K., Chao, K., Quinn, B.C., Yao, P., 1997. Postmortem cryosectioning as an anatomic reference for human brain mapping. *Comput. Med. Imaging Graph.* 21 (2), 131–141.
- Van Buren, J.M., Borke, R.C., 1972. Variations and Connections of the Human Thalamus. Springer-Verlag, New York.
- Watkins, A.J., 1969. A Stereotaxic Atlas of the Human Thalamus and Adjacent Structures. A Variability Study. Williams and Watkins, Baltimore.
- Xu, M., Nowinski, W.L., 2001. Talairach-Tournoux brain atlas registration using a metalforming principle-based finite element method. *Med. Image Anal.* 5 (4), 271–279.